Mountain permafrost landslides: Experimental study investigating molard formation processes

Calvin Beck [a,*], Marianne Font [a], Susan J. Conway [b], Meven Philippe [b,c], Jérémiah Clément [a], Costanza Morino [c,d]

[a] *Normandie Université, UNICAEN - UNIROUEN, CNRS, UMR 6143 M2C, Laboratoire Morphodynamique Continentale et Côtière, Caen, France*
[b] *Nantes Université, Univ Angers, Le Mans Université, CNRS, Laboratoire de Planétologie et Géosciences, LPG UMR 6112, 44000 Nantes, France*
[c] *Université Savoie Mont Blanc, CNRS UMR 5204, Laboratoire Environnements, Dynamiques et Territoires de la Montagne, France*
[d] *University of Padova, Department of Land, Environment, Agriculture and Forestry, Padova, Italy*

ARTICLE INFO

ABSTRACT

Landslides triggered by degrading mountain permafrost pose an increasing risk to life and infrastructure in mountain regions due to current climate change trends. Because discontinuous mountain permafrost is not directly detectable by remote sensing, permafrost molards offer a way of indirectly detecting its location and state. Permafrost molards are cones of loose debris that are associated with landslide deposits. They originate from ice-cemented blocks of sediment that are transported downslope with the landslide. These ice-cemented blocks are fragmented parts of the permafrost initially located in the landslide source area. Over time, these blocks degrade into conical mounds with diameters typically ranging from decimeters up to 40 m. They indicate the presence of an area of degrading permafrost at the level of the detachment zone. The physical processes that lead to the formation of molards from the ice-cemented blocks have not yet been studied in detail. Therefore, we perform an experimental study to recreate molards in a controlled laboratory environment and investigate the key formation processes. We downscale the molards to an initial cube side length of ~30 cm, and reduced the model's complexity by using two different types of gravel with a defined granulometry and lithology. We quantified the degradation phase by using a novel photogrammetric time-lapse system to detect changes in the digital elevation model between half-hourly time-steps. For the first time, we successfully recreated morphologies resembling molards under controlled laboratory conditions on a decimeter scale. We find the main processes to produce the final molard shape are cascades of grainfall for slightly cohesive sediment, and individual grainfall for non-cohesive sediment. Our experiments reveal three possible cross-section shapes (bell-shaped, triangular, trapezoidal) that correspond to molards that can be found in the field. Along with these field observations, we suggest that it may be possible to identify the cohesion of a molard's sediment based on its morphology. Together with future field data and experiments investigating the granulometry, ice and clay contents of the initial ice-cemented block, we aim to use molards as a record to better understand the landslide dynamics and state of the mountain permafrost.

1. Introduction

Permafrost plays a crucial role in stabilizing mountain ranges in polar and high-mountain regions (e.g., Deline et al., 2015). Global warming trends since the end of the 20*th* century have resulted in an increasing degradation of permafrost (e.g., Haeberli et al., 1993; Zhao and Wu, 2019). This results in a destabilization of mountain faces especially in zones of discontinuous permafrost (e.g., Gruber and Haeberli, 2007; Krautblatter et al., 2013; Patton et al., 2019; Deline et al., 2021; Sæmundsson et al., 2022). These potential slope movements occur

at high elevation and/or in remote regions among others in the Andes Mountain Range (e.g., Tapia Baldis and Trombotto Liaudat, 2019), Canada (e.g., Geertsema et al., 2006), the European alps (e.g., Haeberli et al., 2017), and the Himalayas (e.g., Gruber et al., 2017). Because they are extremely unpredictable in terms of dynamics and detachment zones, they pose a serious risk to life and infrastucture even in remote regions. At the same time, permafrost is also an important proxy and component of the global climate system with strong climate feedbacks (e.g., Mauro, 2004; Cheng et al., 2022). Although permafrost extent can be numerically modeled (e.g., Riseborough et al., 2008; Jafarov et al.,

2012; Etzelmüller et al., 2020), in zones of discontinuous permafrost its spatial and temporal heterogeneity presents a major challenge for obtaining precise estimations. However, landforms called permafrost molards associated with landslide deposits can be used to indicate that discontinuous permafrost was present in the mountainside before its failure (Morino et al., 2019). For simplicity we will refer to permafrost molards as molards throughout the rest of this publication.

Molards are cones of loose debris typically ranging from 0.3 to 12 m in height, and up to 40 m in diameter (Milana, 2016; Sæmundsson et al., 2018; Morino et al., 2019; Fernández-Fernández et al., 2023). They originate from ice-cemented blocks of sediment that are transported downslope with the landslide. These often cuboid shaped blocks can survive impacts with surrounding landslide material, topography and vegetation during their transport and come to rest at lower altitudes. The displacement of the blocks to a warmer and more exposed setting (see Fig. 1a) results in ice melt, or sublimation under arid conditions. With time these initial blocks degrade into the conical mounds of loose debris (Fig. 1b) which are then referred to as molards (Goguel and Pachoud, 1972).

The typical molard flank angles are reported by Cassie et al. (1988) and Milana (2016) to correspond to the angle of repose for the respective material. Molards can be found in geographically and geologically diverse regions such as Alaska (Jacquemart et al., 2022), Argentina (Milana, 2016), Canada (Geertsema et al., 2006), Colorado (Allstadt et al., 2023), the European Alps (Goguel and Pachoud, 1972), Greenland (Svennevig et al., 2023) and Iceland (Morino et al., 2019). From field site to field site, the number of molards per landslide, their distribution, and their shape parameters are very variable. Some sites only have a few isolated molards where as other sites have large fields of molards. The shape parameters vary in terms of the cross-sectional shapes, symmetry, eccentricity, flank angles and basal slope angles (Milana, 2016; Morino et al., 2019). Furthermore, potential molard candidates have been found on other planetary bodys such as on Mars and Mercury (Wright et al., 2020; Morino et al., 2023).

Permafrost molards are a useful geomorphological feature to quickly detect the recent or past history of permafrost degradation of a slope from field- or remote-sensing data. However, to date, molards have not been used to give detailed information about the ground ice content of the mobilized material, except in extremely rare cases where the initial frozen blocks were observed immediately after the failure (Brideau et al., 2009; Sæmundsson et al., 2018; Svennevig et al., 2022; Allstadt et al., 2023). With the exception of the study by Allstadt et al. (2023), the timescale the frozen block requires to degrade into a molard remains largely unconstrained. However, in order to explore these two open questions the processes that lead to molard formation need to be better understood. Therefore, the principal goal of this study is to determine if it is possible to recreate molards under controlled laboratory conditions and to then determine the key molard formation processes. By performing laboratory experiments we can study a large parameter space under controlled conditions and isolate processes, which would not be possible by remote sensing or fieldwork. We aim to investigate the temporal distribution of these processes and their contribution to the final molard shape for two different types of idealized sediment. We then qualitatively compare the cross-sections of the artificial molards to those of molards that can be found in two examples of landslides producing molards with contrasting shapes (Subsection 2). Also, we investigate how different height-to-width ratios of the initial ice-cemented block of sediment and the average thawing temperatures affect the molard formation processes and, therefore, its final shape. Finally, we put our results in context of what has already been published and highlight the implications of our work on understanding the state of mountain permafrost by studying molards.

2. Setting

Móafellshyrna and Eyjafirði landslides (Figs. 1, 2) are two examples of landslides producing molards, located in central-north Iceland. Both landslides are located in regions of Tertiary Basalt Formation (Miocene-Lower Pliocene) (Jóhannesson, 2014). The Móafellshyrna landslide occurred on the 20th September 2012 on the west slope of the Móafellshyrna mountain on the Tröllaskagi peninsula (65°55′4.42″N, 18°56′7.13″W). The mountain has an height of 1044 m.a.s.l. with a narrow, north-south divided alpine ridge in a zone with discontinuous permafrost (Etzelmüller et al., 2007). The source material detached from the main scarp at 875–825 m.a.s.l. and some material remained on a topographic bench at 790 m.a.s.l. It transported ~310,000 m^3 of material (Morino et al., 2019), mobilizing tens of meter-scale frozen blocks of sediment (Fig. 12), with one very large block (Fig. 1) of ~11 m in width, degrading into molards over time. Intense precipitation occurred prior to the mass failure with permafrost degradation being the main triggering factor and seismic activity playing only a minor role in the release (Sæmundsson et al., 2018). The landslide is described in detail by Morino (2018). Eyjafirði landslide occurred on the 6th October 2020 on the east slope of the Hleiðargarðsfjall mountain (65°24′10.46″N 18°15′54.38″W). This failure was released at ~880 m.a.s.l. and advanced ~1750 m down slope flowing around farms and a resulting mudslide blocking a regional road, as reported by the Icelandic National Broadcasting Service RUV (Óðinsson, 2020). Aerial pictures published by the news outlet indicate the mudslide might be a secondary event because it is only visible on later images. There was not any heavy rainfall prior to the mass failure, but individual rockfalls in the days leading up to the slope failure which indicate a potential precursory slope movement as reported by local farmer Birgir H. Árason in the Icelandic news outlet Morgunblaðið (Jónsson, 2020).

For the two example landslides the frozen blocks of sediment were displaced <400 and 660 m in altitude for Móafellshyrna and Eyjafirði landslides respectively. With the saturated adiabatic lapse rate of −6.5 K km^{-1} (Hodgkins et al., 2012) and the displacement of the blocks by 600 m in altitude would result in an approx. 4.3 °C warmer climate. The positive air temperature forcing can vary by >15 °C depending on the seasonal timing of the slope failure (Sæmundsson et al., 2018).
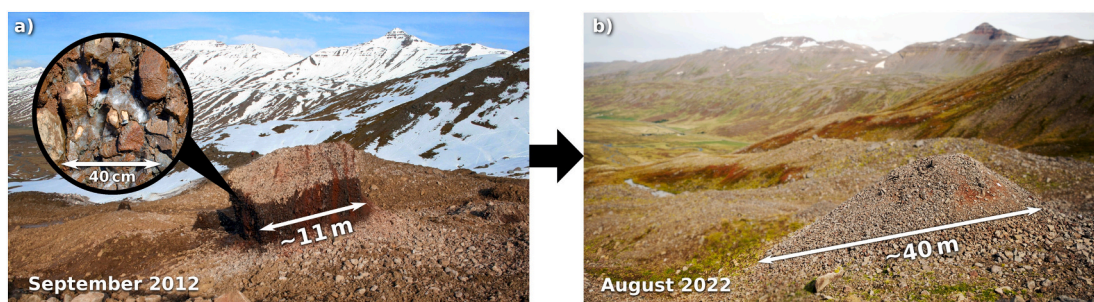

Fig. 1. Images of initially frozen block of sediment in Móafellshyrna landslide (Iceland) deposits, before (left) and after (right) degradation, taken 10 years apart. (a) The initial photograph (courtesy of G. Hansson) was taken one day after the slope failure occurred. (b) With a width of ~40 m, this is the currently largest confirmed molard in Iceland. Coordinates: 65° 55′4.42″N, 18° 56′7.13″W.
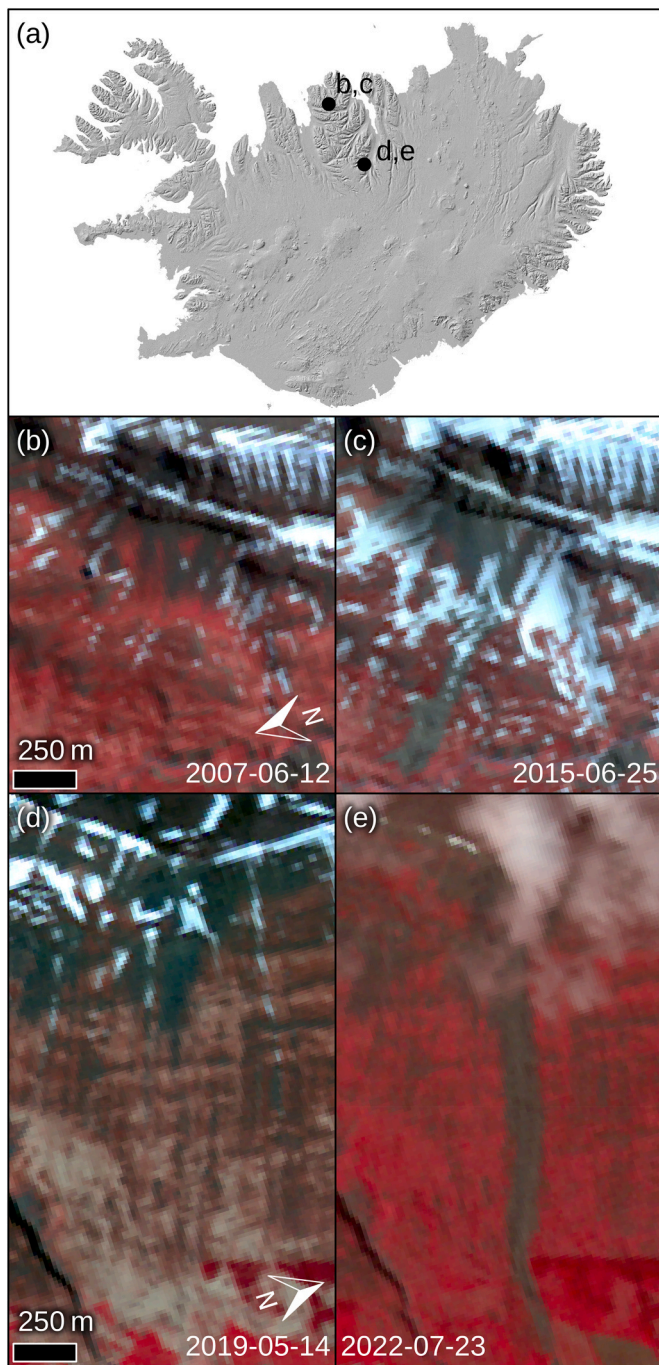
Fig. 2. ASTER false color images of Móafellshyrna landslide site, **(a)** before *(ID: 706121303091305309002)*, and **(b)** after *(ID: 1506251310191506269003)* the slope failure, as well as Eyjafirði landslide site **(c)** before *(ID: 1905141251171905159002)*, and **(d)** after *(ID: 2207231250372207249001)* the slope failure.

3. Material and methods

The following experiments were carried out at the cold chamber facilities of the Continental and Coastal Morphodynamics Laboratory of the French National Centre for Scientific Research in Caen, France. The facility consists of two separate cooling chambers of which one is used for freezing the initial cubic blocks of sediment (Section 3.1) and the other is used for thawing these blocks under controlled conditions (Section 3.2).

3.1. Preparation of initial ice-cemented block

We have followed the generally accepted methods (Harris et al., 2008; Rivière et al., 2019; Costard et al., 2021, 2024) to build an initial block of frozen sediment resembling the permafrost blocks observed in the field (Fig. 1). We prepared this block at room temperature outside of the cooling chamber. We used a wooden cuboidal mold made with an inner dimension of 30x30x32 cm (w x d x h). We selected a cuboid mold shape for practical experimental reasons and because the initial frozen blocks of deposits often have cuboid like shapes e.g. Fig. 1 (Morino et al., 2019). For easier retrieval of the ice-cemented block after freezing, the walls are dismountable and are made out of waxed screen printing plates. The walls were screwed together and the gaps were filled with silicone sealant. After the silicone has dried out, we filled the mold with one of two types of gravel (see Subsection 3.4) and fully filled the pore space (Table 1) with water to the top of the sediment. For practical experimental reasons we kept the ice content constant for each of the two sediments, which is determined by the material's pore space (Table 1). From field photographs of the initial frozen blocks at Moa-fellshyrna landslide (Fig. 1) we determined full saturation as a valid starting point for our experiments. The filled up mold was transported into the freezing chamber on a roller board where it was set to freeze at −20.0 °C. The actual temperature of the cooling chamber periodically cycles with ±1.0 °C around the set point. After a minimum of 50 h the block was retrieved from the freezing chamber and the surrounding mold was dismounted. This freezing duration was determined by initial experiments with wireless temperature sensors (Subsection 3.3) positioned in the sediment block. The temperature sensor with the maximum temperature reached a constant temperature of approx. −19.5 °C after 40–48 h depending on the sediment. Due to the phase change related volume expansion of water, there was a pressure build up in the mold resulting in an ice hump forming either at the top or bottom of the block. The strong temperature forcing hereby reduces ice segregation. This hump was mechanically removed by a hammer as far as possible, to obtain a cuboid shape. However, this inter-experimental variability is a potential source of uncertainty. The now created initial block of frozen sediment was transported to the thawing chamber. The dismounting and transport procedure takes sufficiently little time (< 10 min) for the block's surface not to thaw.

3.2. Degradation phase

The initial ice-cemented blocks were placed in the thawing chamber to study their degradation. The chamber's size allowed us to run two experiments in parallel. Therefore two initial ice-cemented blocks were placed each in the center of a 100 × 90 cm wooden board (Fig. 5A, F). These two boards were connected to each other by steel rods and were equipped with horizontal and vertical markers to provide a single reference frame for photogrammetry. The marker positions were

Table 1
Table of pore-space for very fine gravel and medium gravel under different initial conditions.

	very fine gravel	medium gravel
Initially dry	35 %	44 %
Initially wet	39 %	49 %
Initially wet (after transport)	36 %	45 %

manually measured with a tape measure with a accuracy of ±1 mm. The aim is to keep the forcing for air temperature, humidity, air pressure and radiative forcing as constant as possible. The chamber's air temperature could be modified by the chambers cooling system as well as by an electric heater. The air stream of either was deflected away from the experiments. The heating or cooling is started once the frozen blocks of sediment are placed on the experimental boards. Because the heater is less powerful it reaches its set temperature of 40 °C after 10 h whereas the cooling system reaches the set temperature of 4 °C after 2.5 h. The experiments at room temperature therefore show the most constant temperature and humidity values. However, inserting the frozen blocks into the chamber slightly reduces the air temperature locally by 2–3 °C, because the weather station is positioned ~50 cm away from the degrading block. To keep humidity levels as constant as possible during thawing the wooden boards were placed in a sandpit to absorb the run-off water. Otherwise there was no active humidity and air pressure control available.

3.3. Instrumentation

During the freezing phase of the test run, we placed a wireless temperature sensor (iButton) in the center of the sediment to determine when the frozen block was in a thermally steady state. These devices with model number DS1921G have a temperature range from −40 to +85 °C with a precision of ±1 °C. To protect the sensors during freezing they are encapsulated in a cylinder shaped plastic housing with a height of 2.7 cm and diameter 2.5 cm. Because of the large size of the housing relative to the average sediment diameter, the sensors were only used during the test run to determine the required freezing temperature, because otherwise they would alter the final morphology. At the beginning and end of each experimental run we manually obtained a minimum of 40 photographs from different perspectives with a DSLR (Canon EOS 600D, Canon EF 17-40 mm F/4.0 L) to perform structure from motion (SfM) photogrammetry (Ullman, 1979; Westoby et al., 2012). Additionally we implemented a timelapse photogrammetry setup to continuously monitor the block morphology during the degradation phase at a 30-min interval. The setup consisted of 18 individual rasp-berry PI camera modules mounted on rods approximately 2 m above the boards pointing inward towards the two degrading blocks. A main raspberry PI unit controlled the slave PI cameras and read out the image data via an Ethernet connection. The setup was first presented by Phil-ippe et al. (2021). The processing of these images is discussed in Sub-section 3.5. This setup allows us to track mass transport processes between each 30-min time-step. A mobile weather station was used to monitor air temperature, humidity, and air pressure to validate a rela-tively constant atmospheric forcing.

3.4. Sediment characterization

For the initial experiments, two idealized sediment types were selected based on scaling of field observations to an initial block size of ~30 cm and under consideration of local availability during the COVID-19 pandemic. We used very fine gravel 2–3 mm (Hawaiian quartz) with a low sphericity, angular shape, as well as medium gravel 4–8 mm (Carrara marble) with an elongated subangular shape (Wentworth, 1922; Arculus et al., 2015). The detailed granulometry is displayed in Fig. B.3 in the appendix. Field studies by Morino et al. (2019) show the natural vari-ability of molard sediment with diverse shape parameters, gran-ulometries and clay contents. The simplified sediment cannot account for this wide range of parameters but should provide reduced complexity results.

3.4.1. Pore space

To determine the pore space of the two sediment types we used a scale and Archimedes's principal. We measure the sediment's mass m ($\sigma_m = 0.02$ kg) in a container of determined volume V ($\sigma_V = 2\%$). Then

we filled the pore space with water ($\sigma_{\rho(H2O)} = 0.05\%$) and obtained the combined mass of sediment and water m_w. We then calculated the pore-space s as follows:

$$s = \frac{m - m_w}{\rho_w \cdot V} \tag{1}$$

This measurement was performed with initially dry as well as with initially wet sediment because the pore space expands for wet sediment. The wet sediment was obtained by fully saturating the pore space and then draining the excess water not bound to the sediment. This hygro-scopic, membrane and capillary water increases the mass of the decompacted sediment by 10.1 % and 9.4 % for very fine gravel and medium gravel, respectively. The third measurement was made with initially wet sediment but after transport to the chamber. Due to the vibrations from the transport with the trolley over the tiles the sediment compacts. The results are displayed in Table 1.

Based on error propagation from Eq. 1 we calculate an uncertainty of ±1 % on the estimated pore space values. We used the water density at 0 °C of 999.9 kg m^{-3} and the ice density at −20 °C of 919.4 kg m^{-3} to calculate the ice content within the block of sediment (Vedamuthu et al., 1994; Harvey, 2019). Therefore the volume increased by ~8.8 %, resulting in an ice quantity of the final blocks of initially dry very fine gravel and medium gravel of 38 % and 48 %, respectively.

3.4.2. Angle of repose

Because field observations by Brideau et al. (2009); Milana (2016) and Morino et al. (2019) imply that the sediments angle of repose (AOR) is a critical parameter for the final shape of the molard, we estimated this value for both sediment types. We applied two different methods adapting from Al-Hashemi and Al-Amoudi (2018):

3.4.2.1. Slope angle variation. A tray was filled with each sediment individually and the angle of the tray was slowly raised with a scissor jack until a slope failure occurs. The tray surface was equipped with a grid of smaller metal trays (3 cm high, 11 cm wide) to prevent basal sliding and was dimensioned in a way that the layer height dominates over the individual grain size. We used a digital inclinometer with a precision of ±0.2° to determine the static and dynamic AOR of each sediment (Fig. 3). For the static angle of repose the angle of the tray was measured. For the dynamic angle of repose after the slope failure the slope angle was measured at a minimum of 6 representative locations on the slope and averaged to account for variability in the slope. The effective uncertainty of the measurement was larger than the precision of the inclination as placing the inclinometer can slightly disturb the slope additionally to the variability within the slope.
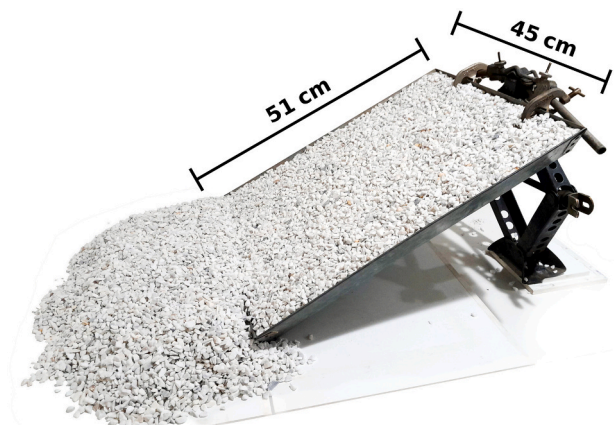

Fig. 3. Static and dynamic AOR estimation via slope angle increase of a metal tray with a scissor jack. Extra sediment is placed in-front of the tray to form a flat run-out surface. Several smaller 3 cm high metal trays are mounted on the surface of the big metal tray to prevent basal sliding.

3.4.2.2. Box lifting. We placed the wooden mold which was used to create the initial frozen blocks with the bottom element removed on the experimental platform and fill it with sediment. Then we slowly (approx. 2 cm s^{-1}) lifted the mold resulting in the individual grains being dynamically released and thus we obtained the dynamic AOR from the displaced sediment (Fig. 4).

We performed duplicates of these experiments for dry and wet sediments. For the wet sediment we filled the sediment pore space with water and let the excess water drain. We used the same digital inclinometer as in the previous method and average over a minimum of 6 representative locations on the slope. Additionally, we manually took pictures from different perspectives to process a digital elevation model as described in Subsection 3.5. The results are displayed in Table 2.

3.5. Data processing

We used Agisoft Metashape *Version 1.7.6* to process the photographs into a digital elevation models (DEMs) by using structure from motion (SfM) photogrammetry (Ullman, 1979; Westoby et al., 2012). We processed the models for the time-steps of each experimental run in batch and derived the maximum block height, its volume and rotationally averaged cross-sections from the DEMs. For the individual processing steps and tools refer to Appendix A.1.

4. Results

In total we degraded 18 blocks of ice-cemented sediment with one experimental run requiring a minimum of each two days for freezing and thawing the block. Thawing the initially frozen blocks of sediment results in conical mounds of loose debris resembling molard shapes that can be observed in the field.

4.1. Dominant processes

We divided the thawing period of the initial frozen block of sediment in to the following four phases. The timing of each phase varies by sediment type, size and temperature forcing.

4.1.1. Surface and excess ice melt
The smooth surface layer of ice on the sides of the block (Fig. 5A, F) melts until the sediment is exposed. The initial block's imperfections, such as ice humps at the block's base, result in parts of the initial block not being in contact to the wooden platform. These air gaps between the initial block and the platform diminish as the base of the block melts away. This can result in a sudden non-mass-wasting-related volume and height change in the DEM.

Fig. 4. Dynamic AOR estimation by slowly lifting a wooden mold filled with sediment. The same 30 × 30 cm mold was used as for creating the initial frozen blocks of sediment but with a removed bottom plate. The mold was lifted at roughly 2 cm per second.

Table 2
Table of static and dynamic angle (°) of repose (AOR) for very fine gravel and medium gravel by measurement method.

sediment	release type	dry/wet	°static	°dynamic	°dynamic.std
very fine gravel	box lifting	dry	-	26	2
	inclining slope		37	31	2
	box		-	26	3
	lifting	wet	-	30	6
	inclining		51	29	4
	slope		50	30	3
medium gravel	box		-	34	2
	lifting	dry	-	35	2
	inclining		46	33	1
	slope		47	34	1
	box		-	28	2
	lifting	wet	-	31	5
	inclining		48	31	2
	slope		47	34	3

4.1.2. Center column degradation phase
Mass movements start at the corners of the block, then at the edges and later on the faces of the block (Fig. 5B, G). Sediment detaches either as grain avalanches or individual grains depending on the sediment (see Subsection 4.2). A ring of sediment forms around the block, which, over time, creates a conical shape from the ground up (Fig. 5C, H). The center column then slowly transforms from a cuboid to square frustum with rounded edges. The maximum height only lowers very slowly during this phase.

4.1.3. Transition phase
For initial blocks with a certain height-to-width ratio (see Subsection 4.5) the center column transforms into a cone merging into the surrounding cone of sediment (between Fig. 5D-E and H-I). The maximum height of the block drastically drops during this phase. Based on visual inspection of the timelapse images we identify that for the sediment to fully degrade the remaining undegraded sections have to dry up first as the sediment is only cohesive while wet.

4.1.4. Settling phase
In the last phase, single grains slowly settle without macroscopic mass movements as remaining pore ice melts, and the sediment reduces its pore space by settling (between Fig. 5 I-J). This is enhanced as the sediment dries up and loses its cohesion and therefore pore space (Section 3.4).

4.2. Influence of granulometry

The two selected sediments produce different results in terms of their final morphology, dominant mass wasting processes and timing. For the very fine gravel the dominant process during phase II of the molard formation is by grain avalanches. This is displayed in Fig. 6 by difference maps between two hourly time-steps of DEMs. The source and sink areas are clearly locally defined. These grain avalanches are temporally variable and vary in terms of mass transported per release event (Fig. 7c). The block of frozen medium gravel in contrast degrades by individual grain-fall. Fig. 7c shows the volume transport by time and therefore indicates that for the medium gravel the degradation is more continuous whereas the grain avalanches of the very fine gravel result in more variability between time-steps.

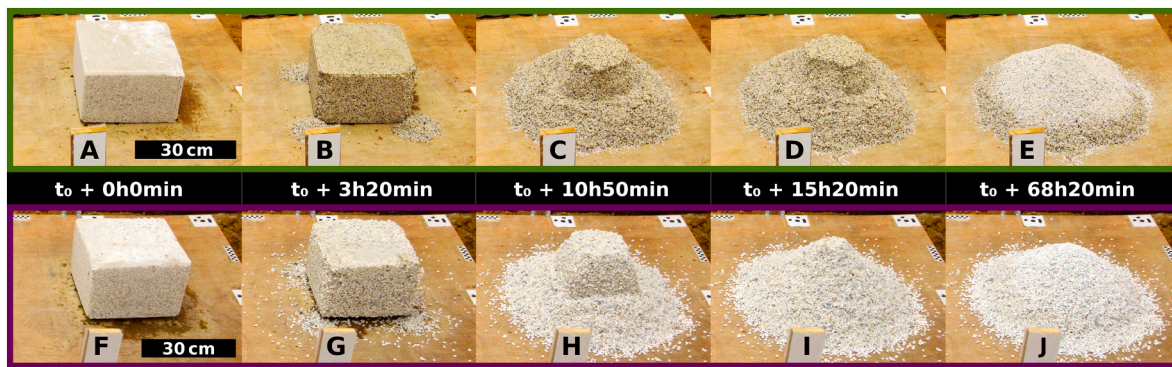In general the very fine gravel takes longer to degrade, however, the key

Fig. 5. Degradation of initial frozen block of sediment (EXP6) at different time-steps for both the very fine and medium gravel. We obtain a final conical mound of loose sediment. For time-lapse video see the video supplement.
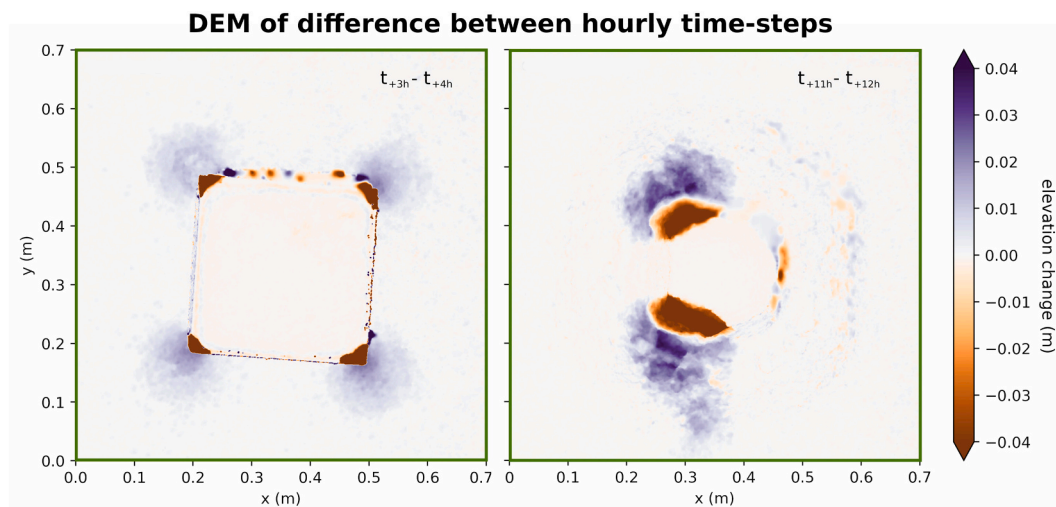

Fig. 6. Two examples of DEMs of difference between hourly time-steps for the very fine gravel (EXP6b). Dark orange colors correspond to zones of mass loss (source) and blue colors correspond to zones of mass gain (sink).

difference in terms of its shape is the transition between the center column degradation phase (IIa) and the merging phase (IIb) (Fig. 5D, Fig. 7). The center column remains stable for longer and then rapidly degrades as the sediment dries out. This results in a sudden drop in height in contrast to the medium gravel where the height lowers continuously in the merging phase (IIa) (Fig. 7A). For both sediments the volume initially decreases as air gaps between the board and the frozen block melt away (Fig. 7B). For the medium gravel this trend continues, however for the very fine gravel the volume expands during the center column degradation phase.

4.3. Molard slope angle vs. angle of repose

We compare the rotationally averaged cross-sections of the degraded blocks of initially frozen sediment resembling molards with the rotationally averaged cross-sections of the released sediment from the lifting box experiment (Section 3.4.2). In the box lifting experiment when the grains exit the box they build up a rim from inside out around the box. The released sediment forms a slope for the subsequent sediment to flow down when exiting the box. For the experiment where we degrade an initially frozen block of ice cemented sediment individual grains detach from the block as the ice melts or grain avalanches occur. Individual grains that detach from the ice-cemented block of sediment are transported the furthest away the higher and closer to the edges they were initially located in the frozen block. This results in several grains being displaced far enough to not be in contact with the final molard after its

final degradation. Grain avalanches that detach from the ice-cemented block of sediment also form a rim around the initial block that thickens and transitions into a cone over time. For both methods the very fine gravel produces constant slope angles over most of the cross-section area whereas the medium gravel produces a more a bell-shaped cross-section. Wet sediment shows a larger spatial variability than dry sediment as displayed in Fig. 8 by the larger standard-deviation (shadowed area). The wet very fine gravel decompacts during the release process resulting in an volume increase. The flank angle of the degraded blocks of initially frozen sediment resembling a molard is steeper for both sediments then their wet and dry dynamic angle of repose. For the very fine gravel the molard flank is about 8° steeper than the material's dry and wet angle of repose. The medium gravel's wet AOR maximum value reaches up to the slope angle for a molard made of the same material. However, of average the molard flank is steeper than the material's wet angle of repose.

4.4. Average temperature variation

To investigate how the average thawing temperature impacts the molard formation processes and its final shape, we perform experiments at each 4 °C, 17 °C, and 35 °C average temperature. The temperature and humidity timeseries for each experiment are displayed in the appendix in Fig. B.2. Independent of the thawing temperature, the rotationally averaged cross-sections (Fig. 9) show indistinguishable results within experimental variability which corresponds to variations in the height of the initial block.
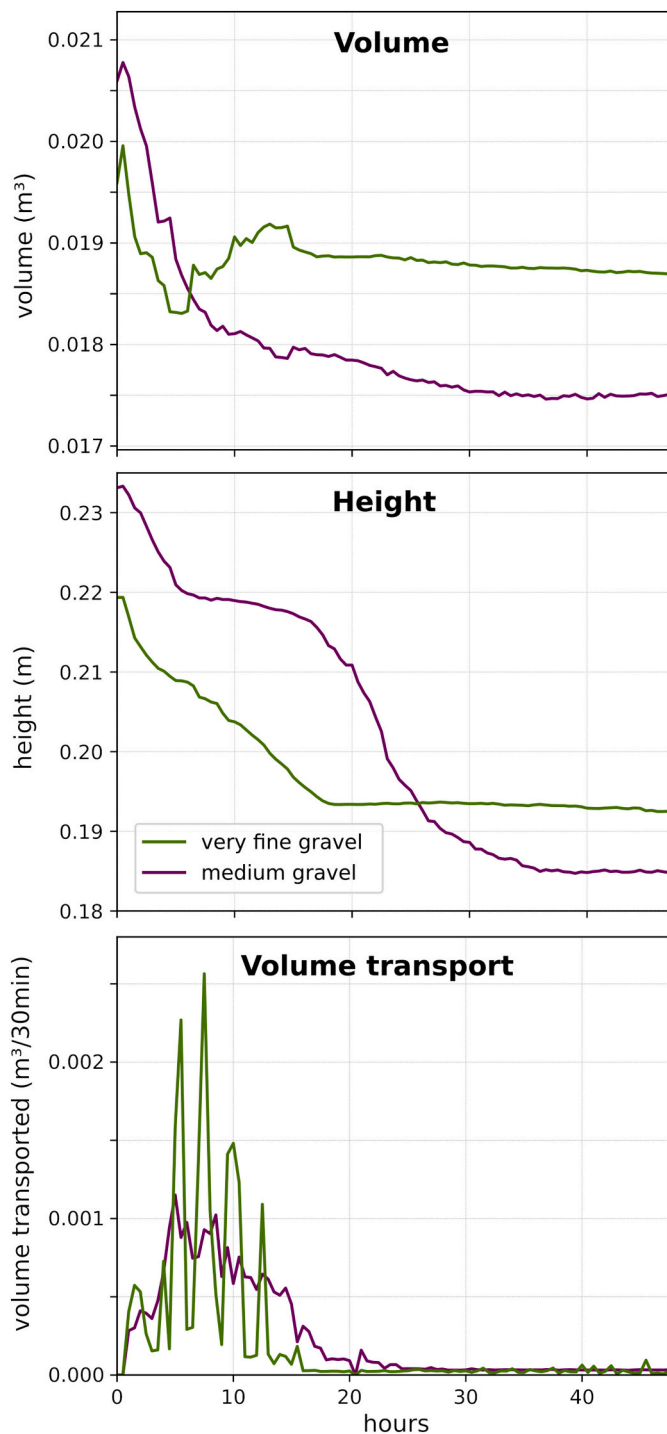
Fig. 7. Timelines of absolute sediment volume (top), maximum vertical sediment height (center), and sediment volume transport (bottom) for EXP6 (see Table B.1).

Even though the time the frozen ice-cemented blocks require for degrading reduces for increasing average temperatures, the types of processes and phases remain comparable for the respective sediment type. The volume transport curves (Fig. 10) show a comparable enough behavior to distinguish between the respective sediment types. The curve of the very fine gravel is steeper and higher, whereas the curve for the medium gravel is wider and shallower. The characteristic fluctuating curve cannot be observed in this figure for the very fine gravel, because due to the resampling the time-steps duration is much longer than the time between the processes. Time-lapse videos of the blocks degrading under all
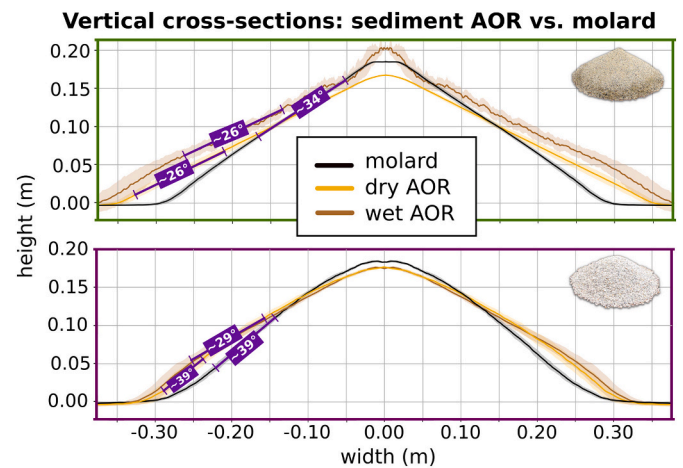

Fig. 8. Rotationally averaged cross-sections of degraded initially frozen block of sediment (molards, EXP6) and lifted box filled with dry or wet sediment for very fine gravel (top) medium gravel (bottom). The shadow represents the standard deviation for the rotationally averaged region. The slope angles are indicated for selected sections marked in purple. The degraded ice-cemented blocks show steeper slope angles in comparison to the corresponding angle of repose. Small images of molards indicate respective sediment type of the plot.

three temperature forcings are displayed in the video supplementary material.

4.5. Aspect-ratio variation

We investigate the influence of the initial block aspect ratio by varying its height for a constant square surface area. For the very fine gravel with an initial block higher than the block width, we obtained triangular cross-sections (Fig. 11). For lower aspect ratios the triangular cross-section transition a trapezoidal cross-section, while keeping a constant slope angle within the experimental variability. For the medium gravel we find a bell-shaped like cross-section for all aspect ratios with the peak flatting for lower aspect ratios. The final height of the degraded block is directly correlated with original height of the block. For large height-to-width ratios (yellow, orange, red graphs in Fig. 11) the height decreases more than for low ratios (purple and blue graphs in Fig. 11) where the original block height hardly changes.

5. Discussion

Our experiments are the first to observe the molard key formation processes under quantifiable laboratory conditions on a decimeter scale. In the following section, we evaluate our results with respect to molard field observations and relevant publications. We identify individual grain fall and grain avalanches to be the main processes forming the final molard morphology with the following phases: I. surface and excess ice melt, II. main degradation phase, and a III. settling phase. The two different tested sediment types medium gravel and very fine gravel produce bell-shaped or triangular/trapezoidal cross-section types respectively.

5.1. Air temperature

To cover the range of possible air temperature forcings we degraded the ice-cemented blocks at different average air temperatures (4 °C, 17 °C, 35 °C). The time the initial blocks require to degrade increases with decreasing average air temperature. However, the temperature forcing did not modify the final shape of the molard, because the average thawing temperature only affects the timing but not the degradation processes (Fig. 10). Therefore, studying the formation processes resulting in the degradation of the initial ice-cemented blocks at room temperature is a valid approach. Degrading the ice cemented blocks at room
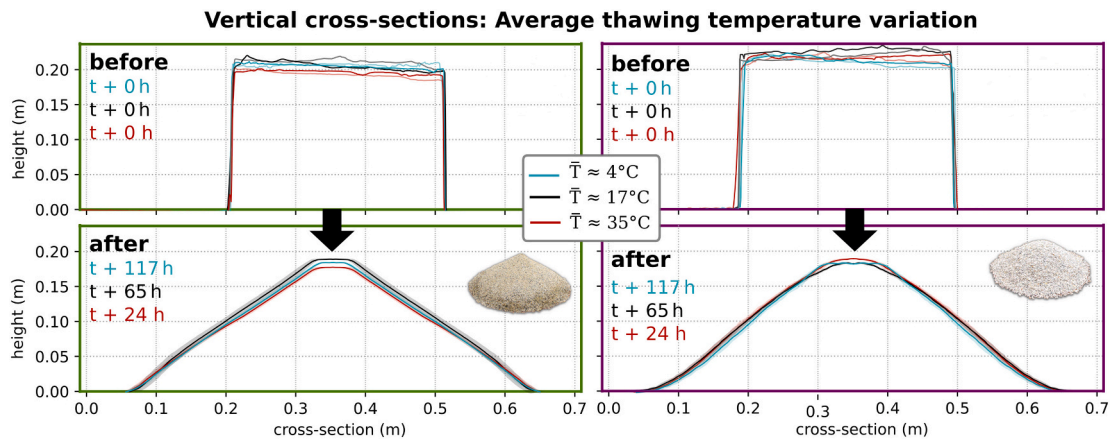
Fig. 9. Vertical before and after cross-section profile comparison for different average degradation temperatures (4 °C, 17 °C, 35 °C) for very fine left and medium gravel right. For the "before" graphs two orthogonal cross-section have been obtained crossing through the block center, parallel to the block faces. For the "after" graphs a rotationally averaged cross-section is displayed. The displayed "after" cross-sections are obtained after different time durations depending on the temperature forcing indicated by the corresponding line color. Data from the experimental runs EXP6, EXP8 and EXP9 have been used to create this figure. Small images of molards indicate respective sediment type of the plot.
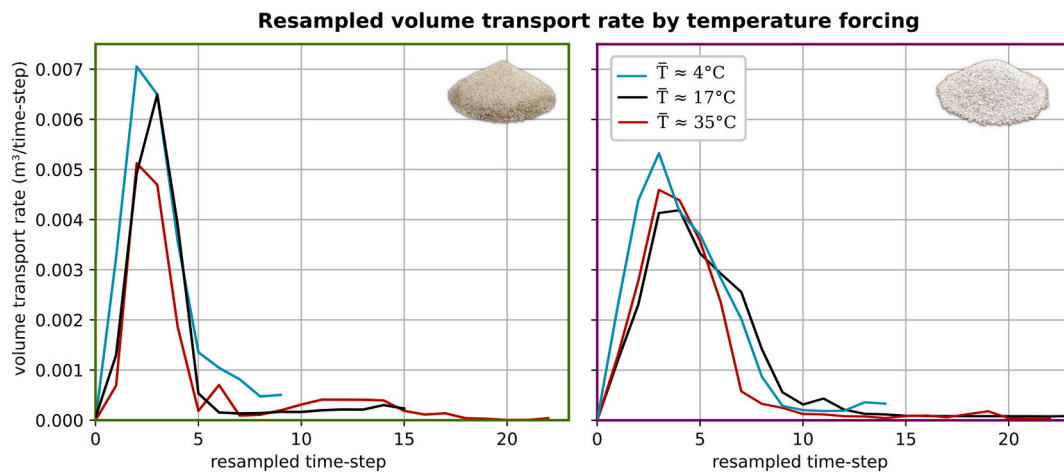

Fig. 10. Volume transport per normalized intervals for very very fine (left) and medium gravel (right) during blocks degradation phase for different air temperature forcings. The data from the 4 °C and 17 °C runs have respectively been temporally re-sampled by a factor 1/12 and 1/3 for very fine gravel and by 1/8 and 1/2 for medium gravel to match the 35 °C curves as far as possible. The data was re-sampled by summing over n time steps, where n corresponds to the denominator in the scaling factor. Data from the experimental runs EXP6, EXP8 and EXP9 have been used to create this figure. Small images of molards indicate respective sediment type of the plot.

temperature (17 °C) is advantageous for experimental reasons because it reduces the experimental duration by half in comparison to the 4 °C forcing.

5.2. Molard slope angle vs. angle of repose

Cassie et al. (1988) and Brideau et al. (2009) observed molards' flanks to rest at the angle of repose. We therefore compared the final molard shape with experimentally determined values of AOR for the respective sediments (Subsection 3.4.2). Both the box lifting and molard type experiments result in conical mounds of sediment. However, molards in our experiments had an up to 10° steeper slope angle compared to the dynamic angle of repose for the respective sediment (Fig. 8). The mass wasting processes during these two experiments is different, because for the box lifting experiment the cone builds up from the bottom to the top with a continuous granular flow forming the final morphology. For the molard type experiment the blocks degrade from the top corners to the bottom by individual grain fall and/or grain avalanches. The higher the position from where the grains detach from the block the more potential energy is available and transformed to kinetic

energy. Therefore, for individual grain fall the first grains to be detached are transported the furthest away from the initial block and remain as an annulus of individual grains around the molard after the block has fully degraded. This does not happen for the box lifting experiment, resulting in a sharp transition between sediment flank and the experimental board. The box lifting and molard like experiment produce the same general cross-section type (bell-shaped, triangular) for the respective sediment. The cross-section type therefore seems to be related to the sediment type and is not very sensitive to the specific grain release caused by the thawing for molards. However further experiments with more sediment types will be necessary to confirm this hypothesis.

5.3. Comparison to molards in the field

The three cross-section types obtained in the lab experiments (bell-shaped, triangular, trapezoidal) can also be observed in the field. However, field molards show a larger diversity in shapes than the experiments (e.g., Brideau et al., 2009; Milana, 2016; Morino et al., 2019) and can consist of individual molards superimposed into each other. Bell-shaped cross-section can be found in the Móafellshyrna landslide
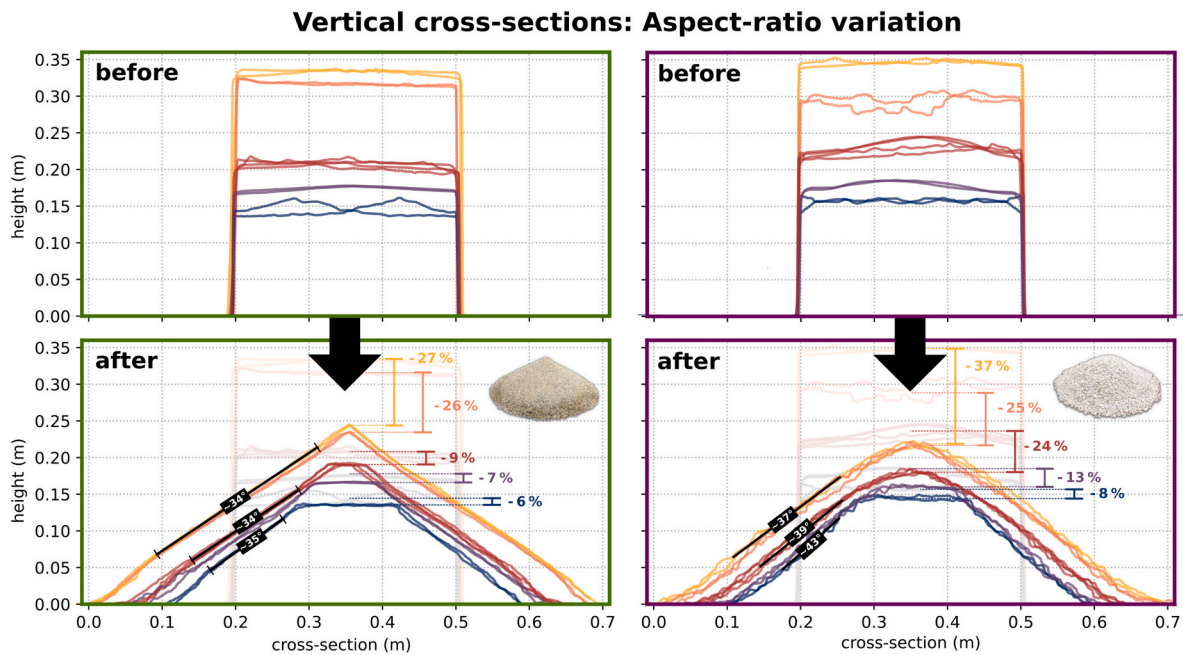
Fig. 11. Vertical before and after cross-section profile comparison for different height-to-width ratios for very fine (left) and medium gravel (right). The base area is kept constant at 30x30cm and only the height is varied. Two orthogonal cross-section have been obtained through the center of the degraded sediment, parallel to the initial block faces. Scales on "after" graph indicate the relative height reduction between the initial height and the degraded block (color coded to the corresponding block). The experimental data from runs EXP2–7 have been used to create this figure. Small images of molards indicate respective sediment type of plot.

(Fig. 12a) and triangular/trapezoidal cross-section can be found in Eyjafirði landslide (Fig. 12b/c).

The bell shaped molards in the Móafellshyrna landslide have a sharp slope transition between the molard flank and surrounding terrain whereas the laboratory experiments show a gradual flank. The annulus that can be observed under laboratory conditions originates from the first grains with the highest potential energy bouncing further away on the wooden board. In the field the soil or landslide material is rougher and less elastic, therefore absorbing the energy and reducing bouncing of the individual grains. Hence, we think this difference can be attributed to the different substrates underneath the experimental and field molards.

5.4. Aspect-ratio

Morino et al. (2019) proposed that the initial width B of the initial block can be estimated by $B = 2\sqrt{L^2 - h^2}$ where L denotes the cone's slant height and h the height of the cone. Our experiments suggest such a simplified approximation is not valid, because the final height h decreases non-linearly with the initial height and forms plateaus for low height-width ratios. Because this property is sediment dependent, we can only determine a minimum height for the initial block, which has to be at least as high as the molard. So molard heights can be used to estimate the minimum thickness of the initially frozen layer in the source

area of the landslide.

5.5. Sediment types

During the main degradation phase (II) the two sediment types very fine gravel and medium gravel show different key formation processes. For the medium gravel the individual grains melt out of the block and fall to the surface one at a time. The individual grains detach at a relatively constant rate and over time and form a molard with a bell-shaped cross-section. For the very fine gravel, grains detach and fall from the block as a grain avalanche forming a triangular to trapezoidal molard shape depending on the initial block's width to height ratio (Fig. 5a). These grain avalanches are temporally variable in terms of mass quantity transported per release event resulting in a curve with greater fluctuations(Fig. 7 (bottom)). However, the very fine gravel takes longer to degrade than the block with the medium gravel. This is because the very fine gravel retains moisture longer in its pore space than the medium gravel due to the liquid bridges between the grains, making the sediment more cohesive (Chen et al., 2018). Estimating the capillarity in bulk sediment is challenging due to its irregularities in void space and contact points therefore creating variable water contents held by these interstices. For the assumption of two spherical grains bonded together by capillary bonding, the pressure difference between the two grains decreases proportional to 1/radius according to Young-Laplace equation (Laplace,

Fig. 12. Images of three individual molards with corresponding idealized cross-sections located in deposits of a) Móafellshyrna landslide, Iceland; b) and c) Eyjafirði landslide, Iceland (see Subsection 2).

1806; Young, 1832). Therefore based on the average sediment diameter of 2.3 and 5.5 cm for the very fine gravel and medium gravel respectively the very fine gravel has more than two times stronger capillary bondings.

5.6. Cohesion

On the small laboratory scale the capillary forces act as a cohesive force as long as the sediment is wet. Because the capillary force decreases with increasing grain radius this force is less relevant for molards of field size. However, the molard sediments in the field can contain clays, providing additional cohesion (Ikari and Kopf, 2011) and therefore strengthens the blocks. From visual inspection of the surface and a small pit in the molards of the Eyjafirði landslide, we observe high quantities of fine sediment filling up the space between the larger cobbles. The Móafellshyrna molards in comparison did not have any fines visible at the surface. This results in voids between the superficial cobble material, indicating overall lower quantities of initial fine materials. The molards with no superficial fines visible produced bell shape cross-sections, whereas the molards with fines visible produced triangular/trapezoidal cross-sections. In the light of our experiments this indicates the possibility of inferring the molard material cohesion based on its cross-section shape.

5.7. Limitations

The properties of clays do not scale, which produces scaling issues for physical modelling of initial blocks with high clay quantities. Also, the impact of liquid precipitation on the degradation of the frozen blocks and its impact on washing out clays has not yet been experimentally studied. Preliminary tests with sediment with high clay contents show that these do not degrade into molards and precipitation is required to mobilize this clay rich sediment into a molard (Fig. B.4). The pressure build-up during the ice formation phase and potential ice segregation have a neglectable effect on the degradation of the blocks, especially when individual grain fall is the dominant process. When grain avalanches are the dominant process anisotropies in the ice structure can affect the distribution of individual grain slide events, but these are not expected to have an influence beyond the experimental variability. The large parameter-space, such as varying clay and ice contents, is not yet accurately represented in our experiments and will be subject to future experiments. Also experiments at different scales will be necessary to confirm the applicability of lab results to the field. These findings will be crucial, because molards still hold a large future potential in determining the state of mountain permafrost, as permafrost molards can even be found in regions where permafrost was not previously expected (Morino et al., 2019).

5.8. Application to other landforms

The findings from our experiments can give insights into the degradation processes of other landforms where both:

- Ice locally stabilizes otherwise loose material in slopes steeper than the material's angle of repose.
- Slope failures result in new ice-cemented material being exposed to the surface.

This can be the case for steep rock glacier fronts (e.g., Delaloye et al., 2010), debris-covered glaciers flowing over steep topographies (e.g., Westoby et al., 2020), exposed permafrost slopes, especially after active layer failures or frost heave steepened loose material (e.g., Rist and Phillips, 2005; Gruber and Haeberli, 2007; Niu et al., 2016) during annual freeze-thaw cycles. Analog to the medium gravel experiments, melting out of individual rocks results in individual rockfall as the key process for decimeter and larger scale debris. However, the hydrologic processes in these systems cannot be accounted for explicitly in our

experiments. Applying the findings from our experiments to landforms with an icy core such as dirt cones or ice-cored moraines is more limited. Dirt cones – even though they result in a comparable final morphology – are a self-regulating system where the superficial debris creeps and thins while the cone grows until it reaches a steady state (e.g., Drewry, 1972; Hénot et al., 2023) therefore remaining at or below the material's angle of repose. Ice-cored moraines show a large heterogeneity of the debris and ice distribution and can contain complex drainage systems transporting latent heat within the moraine (e.g., Johnson, 1971; Krüger and Kjær, 2000; Ewertowski and Tomczyk, 2015). These hydrological processes and potential damming of glacier lakes are not modeled in our experiments.

Future experiments could be easily adapted to a more complex parameter space with variable ice quantities and structures, lithologies, and grain sizes. This would allow a deeper insight into the degradation processes of the landforms described above.

6. Conclusion

From this study the following conclusions can be drawn:

- Hypothesis validation of molards originating from displaced blocks of ice-cemented sediment by recreation decimeter scale molard morphologies in a controlled laboratory environment.
- Sediment types impact molard cross-sections types with bell-shaped or triangular/trapezoidal cross-sections for medium gravel and very fine gravel respectively.
- The average thawing temperature only affects the timing but not the process type of the degradation process.
- The molard flank angles are up to 10° steeper than the investigated material's dynamic angle of repose.
- Grain avalanches and individual grainfall are the main processes producing the molard morphology for very fine gravel and medium gravel respectively.
- Capillary forces play a crucial role in stabilizing the sediment even after all ice has melted.
- No simplified approximation to determine the initial block's height from the degraded molards shape parameters can be identified.

Permafrost molard formation timelapse for RUNS 6,8,9 with different air temperature forcings can be found online at https://doi.org/10.1016/j.geomorph.2024.109317.

CRediT authorship contribution statement

Calvin Beck: Writing – review & editing, Writing – original draft, Visualization, Formal analysis, Data curation. **Marianne Font:** Writing – review & editing, Supervision, Funding acquisition, Conceptualization. **Susan J. Conway:** Writing – review & editing, Supervision, Project administration, Funding acquisition, Conceptualization. **Meven Philippe:** Writing – review & editing, Resources, Data curation. **Jérémiah Clément:** Data curation. **Costanza Morino:** Writing – review & editing, Project administration, Funding acquisition, Data curation.

Declaration of competing interest

The authors declare that they have no conflict of interest.

Data availability

Data will be made available on request.

Acknowledgements

Appendix A. Lab manual

A.1. Appendix A.1. Data processing steps

This section has been moved to the appendix from the methods. We used Agisoft Metashape *Version 1.7.6* to process the photographs into a digital elevation models (DEMs) by using structure from motion (SfM) photogrammetry (Ullman, 1979; Westoby et al., 2012). We use the software's graphical user interface (GUI) for individual models as well as an automatized python script to process a large number of models in a batch. The processing steps are: (0) importing camera images, (1) aligning the images, (2) automatically detecting markers, (3) adding undetected markers, (4) adding positions and scale distances for markers, (5) re-aligning images, (6) aligning chunks for same reference frame, (7) creating a high-resolution dense-cloud, (8) creating a mesh, (9) calculating a DEM based on the mesh, (10) exporting the final DEM. For the automatic processing manually adding undetected markers was not possible and as a substitute, estimated camera positions were imported after step (0). For the automatically generated DEMs with a 0.6 mm/pix resolution we obtained a horizontal marker error of 1 mm and a vertical marker error of 3 mm. To analyze the DEM-timeseries we created and applied a python script to perform the following analysis steps. To import the single DEM GeoTiff files and to convert them to a 2D array we use the packages xarray (Hoyer and Hamman, 2017) which again uses the package rasterio (Gillies, 2019). By summing up the values of the 2D array we calculated volumes and by summing up the difference between 2D arrays of two different time steps we calculated the volume change. To calculate the degrading block's maximum height, we calculate the average value of the 20 highest values with in the 2D array to better reduce the impact of scatter. We used the python package scipy (Virtanen et al., 2020) to interpolate the 2D array to create a re-sampled cross-section. The data was re-sampled along a rotating straight line with the origin at the calculated center of the initial block and radius R rotating a full 360° in 10° intervals to then calculate rotation-averaged cross-sections.

Appendix B. Additional tables and figures

Table B.1
Overview table of experiments.

| ID	Start date	Start (UTC)	Duration (h)	Height (cm)	Sediment
EXP1a	19/04/2021	13:30	51	~30	very fine
EXP1b	19/04/2021	13:30	51	~30	medium
EXP2a	07/02/2022	20:00	72	17-18	very fine
EXP2b	07/02/2022	20:00	72	17-19	medium
EXP3a	10/02/2022	20:00	191	20-21	very fine
EXP3b	10/02/2022	20:00	191	21-22	medium
EXP4a	01/04/2022	20:00	52	30	medium
EXP4b	01/04/2022	20:00	52	30	very fine
EXP5a	11/04/2022	18:30	88	33	medium
EXP5b	11/04/2022	18:30	88	33	very fine
EXP6a	26/04/2022	20:00	69	~20	medium
EXP6b	26/04/2022	20:00	69	~20	very fine
EXP7a	23/05/2022	18:00	86	15	very fine
EXP7b	23/05/2022	18:00	86	15	medium
EXP8a	30/05/2022	19:00	24	20	very fine
EXP8b	30/05/2022	19:00	24	20	medium
EXP9a	02/06/2022	20:00	186	20	medium
EXP9b	02/06/2022	20:00	186	20	very fine

iButton temperature timeseries during freezing
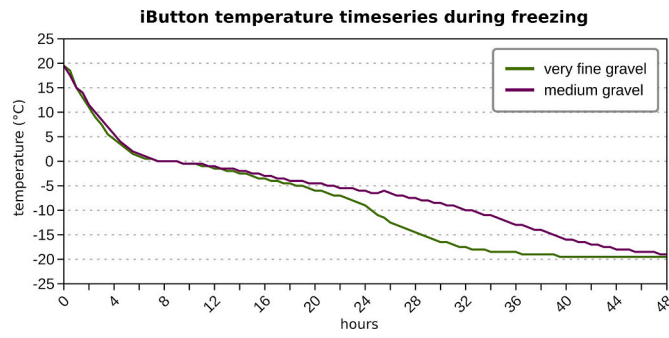
Fig. B.1. iButton temperature timeseries during freezing phase to a minimum temperature of $-20°$ C air temperature (EXP1).

Temperature and relative humidity timeseries

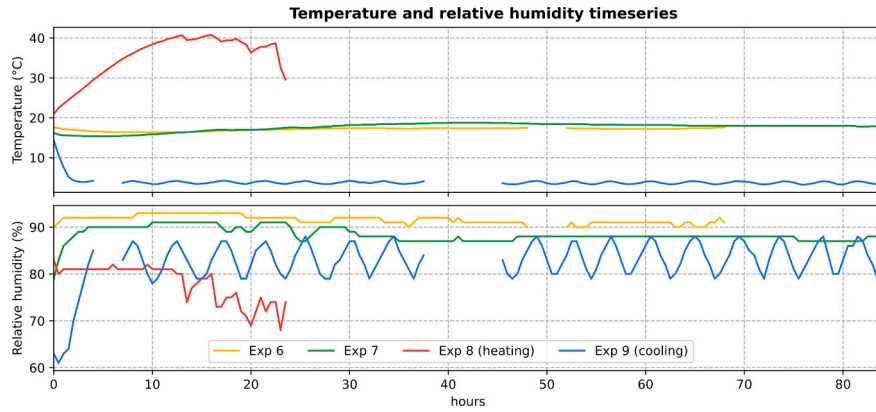**Fig. B.2.** Temperature and relative humidity time-series for experimental runs EXP6 to EXP9. Gaps in the graph are due to data gaps.

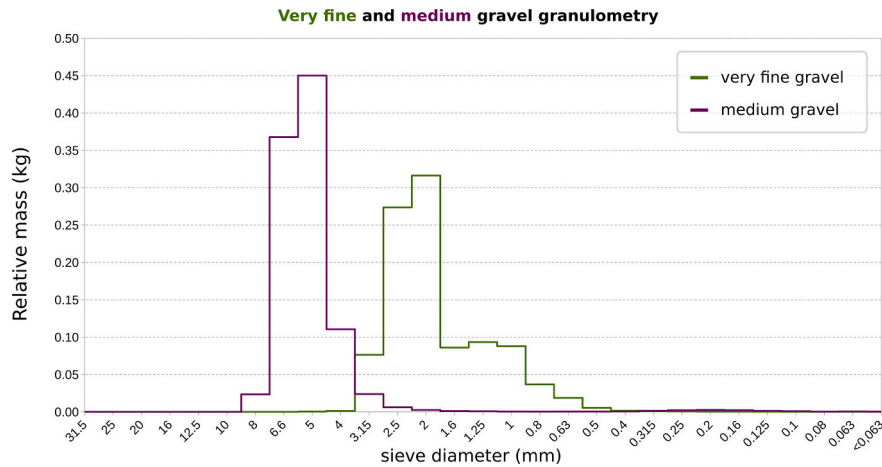**Very fine and medium gravel granulometry**

Fig. B.3. Granulometry of

very fine gravel

and

medium gravel

. The granulometry was obtained by separating and grouping the sample particle size with a sieve shaker and by weighing the sediment contained in each sieve.

Fig. B.4. Photographs of block of initially ice-cemented sediment (left) after 48 h after degradation and (right) after 60 s of simulated precipitation by a watering can. The sediment was obtained from field molard material from the Árnesfjall landslide (Morino et al., 2019).

References

Al-Hashemi, H.M.B., Al-Amoudi, O.S.B., 2018. A review on the angle of repose of granular materials. Powder Technol. 330, 397–417. https://doi.org/10.1016/j.powtec.2018.02.003.

Allstadt, K.E., Coe, J.A., Collins, E.A., Rengers, F.K., Mangeney, A., Esser, S.M., Pursley, J., Yeck, W.L., Bellini, J.J., Brady, L.R., 2023. The 2022 chaos canyon landslide in Colorado: Insights revealed by seismic analysis, field investigations, and remote sensing. Landslides 1–17. https://doi.org/10.1007/s10346-023-02179-4.

Arculus, R., Ishizuka, O., Bogus, K., Aljahdali, M., Bandini-Maeder, A., Barth, A., Brandl, P., do Monte Guerra, R., Drab, L., Gurnis, M., et al., 2015. In: Arculus, R.J., Ishizuka, O., Bogus, K., Expedition 351, The (Eds.), Expedition 351 methods. https://doi.org/10.14379/iodp.proc.351.102.2015.

Brideau, M.A., Stead, D., Lipovsky, P., Jaboyedoff, M., Hopkinson, C., Demuth, M., Barlow, J., Evans, S., Delaney, K., 2009. Preliminary description and slope stability analyses of the 2008 little salmon lake and 2007 mt. Steele landslides, Yukon. Yukon Exploration and Geology 110–133.

Cassie, J., Gassen, W.V., Cruden, D., 1988. Laboratory analogue of the formation of molards, cones of rock-avalanche debris. Geology 16, 735–738. https://doi.org/10.1130/0091-7613(1988)016<0735:LAOTFO>2.3.CO;2.

Chen, J., Williams, K., Chen, W., Shen, J., Ye, F., 2018. A review of moisture migration in bulk material. Part. Sci. Technol. https://doi.org/10.1080/02726351.2018.1504152.

Cheng, F., Garzione, C., Li, X., Salzmann, U., Schwarz, F., Haywood, A.M., Tindall, J., Nie, J., Li, L., Wang, L., et al., 2022. Alpine permafrost could account for a quarter of thawed carbon based on plio-pleistocene paleoclimate analogue. Nat. Commun. 13, 1329. https://doi.org/10.1038/s41467-022-29011-2.

Costard, F., Dupeyrat, L., Séjourné, A., Bouchard, F., Fedorov, A., Saint-Bézar, B., 2021. Retrogressive thaw slumps on ice-rich permafrost under degradation: results from a large-scale laboratory simulation. Geophys. Res. Lett. 48, e2020GL091070 https://doi.org/10.1029/2020GL091070.

Costard, F., Rodriguez, J., Godin, E., Séjourné, A., Kargel, J., 2024. Deciphering martian flood infiltration processes at hebrus valles: Insights from laboratory experiments and remote sensing observations. Journal of Geophysical Research: Planets 129, e2023JE007770. https://doi.org/10.1029/2023JE007770.

Delaloye, R., Lambiel, C., Gärtner-Roer, I., 2010. Overview of rock glacier kinematics research in the swiss alps. Geographica Helvetica 65, 135–145. https://doi.org/10.5194/gh-65-135-2010.

Deline, P., Gruber, S., Delaloye, R., Fischer, L., Geertsema, M., Giardino, M., Hasler, A., Kirkbride, M., Krautblatter, M., Magnin, F., et al., 2015. Ice Loss and Slope Stability in High-Mountain Regions, 521–561. https://doi.org/10.1016/B978-0-12-394849-6.00015-9.

Deline, P., Gruber, S., Amann, F., Bodin, X., Delaloye, R., Failletaz, J., Fischer, L., Geertsema, M., Giardino, M., Hasler, A., et al., 2021. Ice loss from glaciers and permafrost and related slope instability in high-mountain regions. In: Snow and Ice-related Hazards, Risks, and Disasters. Elsevier, pp. 501–540. https://doi.org/10.1016/B978-0-12-817129-5.00015-9.

Drewry, D.J., 1972. A quantitative assessment of dirt-cone dynamics. J. Glaciol. 11, 431–446. https://doi.org/10.3189/S0022143000022383.

Etzelmüller, B., Farbrot, H., Guðmundsson, Á., Humlum, O., Tveito, O.E., Björnsson, H., 2007. The regional distribution of mountain permafrost in Iceland. Permafr. Periglac. Process. 18, 185–199. https://doi.org/10.1002/ppp.583.

Etzelmüller, B., Patton, H., Schomacker, A., Czekirda, J., Girod, L., Hubbard, A., Lilleøren, K.S., Westermann, S., 2020. Icelandic permafrost dynamics since the last glacial maximum–model results and geomorphological implications. Quat. Sci. Rev. 233, 106236 https://doi.org/10.1016/j.quascirev.2020.106236.

Ewertowski, M.W., Tomczyk, A.M., 2015. Quantification of the ice-cored moraines' short-term dynamics in the high-arctic glaciers ebbabreen and ragnarbreen, petuniabukta, svalbard. Geomorphology 234, 211–227. https://doi.org/10.1016/j.geomorph.2015.01.023.

Fernández-Fernández, J.M., Etzelmüller, B., Morino, C., Sæmundsson, 2023. Iceland. In: Periglacial Landscapes of Europe. Springer, pp. 427–473. https://doi.org/10.1007/978-3-031-14895-8_15.

Geertsema, M., Hungr, O., Schwab, J.W., Evans, S.G., 2006. A large rockslide–debris avalanche in cohesive soil at pink mountain, northeastern British columbia, Canada. Eng. Geol. 83, 64–75. https://doi.org/10.1016/j.enggeo.2005.06.025.

Gillies, S., 2019. Rasterio documentation. MapBox: San Francisco, CA, USA 23. URL: https://rasterio.readthedocs.io.

Goguel, J., Pachoud, A., 1972. Géologie et dynamique de l'écroulement du mont granier: dans le massif de chartreuse, en novembre 1248. G.M, B.R.

Gruber, S., Haeberli, W., 2007. Permafrost in steep bedrock slopes and its temperature-related destabilization following climate change. J. Geophys. Res. Earth 112. https://doi.org/10.1029/2006JF000547.

Gruber, S., Fleiner, R., Guegan, E., Panday, P., Schmid, M.O., Stumm, D., Wester, P., Zhang, Y., Zhao, L., 2017. Inferring permafrost and permafrost thaw in the mountains of the hindu kush himalaya region. Cryosphere 11, 81–99. https://doi.org/10.5194/tc-11-81-2017.

Haeberli, W., Guodong, C., Gorbunov, A.P., Harris, S.A., 1993. Mountain permafrost and climatic change. Permafr. Periglac. Process. 4, 165–174. https://doi.org/10.1002/ppp.3430040208.

Haeberli, W., Schaub, Y., Huggel, C., 2017. Increasing risks related to landslides from degrading permafrost into new lakes in de-glaciating mountain ranges. Geomorphology 293, 405–417. https://doi.org/10.1016/j.geomorph.2016.02.009.

Harris, C., Kern-Luetschg, M., Murton, J., Font, M., Davies, M., Smith, F., 2008. Solifluction processes on permafrost and non-permafrost slopes: results of a large-scale laboratory simulation. Permafr. Periglac. Process. 19, 359–378. https://doi.org/10.1002/ppp.630.

Harvey, A.H., 2019. Properties of Ice and Supercooled Water. CRC Handbook of Chemistry and Physics. CRC Press, Boca Raton, FL. URL: https://tsapps.nist.gov/publication/get_pdf.cfm?pub_id=926353.

Hénot, M., Langlois, V.J., Plihon, N., Taberlet, N., 2023. How dirt cones form on glaciers: Field observation, laboratory experiments, and modeling. Phys. Rev. E 107, 034905. https://doi.org/10.1103/PhysRevE.107.034905.

Hodgkins, R., Carr, S., Pálsson, F., Guðmundsson, S., Björnsson, H., 2012. Sensitivity analysis of temperature-index melt simulations to near-surface lapse rates and degree-day factors at vestari-hagafellsjökull, langjökull, Iceland. Hydrol. Process. 26, 3736–3748. https://doi.org/10.1002/hyp.8458.

Hoyer, S., Hamman, J., 2017. Xarray: Nd labeled arrays and datasets in python. Journal of Open Research Software 5. https://xarray.dev/.

Ikari, M.J., Kopf, A.J., 2011. Cohesive strength of clay-rich sediment. Geophys. Res. Lett. 38 https://doi.org/10.1029/2011GL047918.

Jacquemart, M., Welty, E., Leopold, M., Loso, M., Lajoie, L., Tiampo, K., 2022. Geomorphic and sedimentary signatures of catastrophic glacier detachments: a first assessment from flat creek, Alaska. Geomorphology 414, 108376. https://doi.org/10.1016/j.geomorph.2022.108376.

Jafarov, E.E., Marchenko, S.S., Romanovsky, V., 2012. Numerical modeling of permafrost dynamics in Alaska using a high spatial resolution dataset. Cryosphere 6, 613–624. https://doi.org/10.5194/tc-6-613-2012.

Jóhannesson, H., 2014. Geological map of Iceland–bedrock geology–1: 600 000. Accessed online on March 24, 2018.

Johnson, P., 1971. Ice cored moraine formation and degradation, donjek glacier, Yukon territory, Canada. Geogr. Ann. Ser. B 53, 198–202. https://doi.org/10.2307/520789.

Jónsson, J.P., 2020. Þetta var svakalegur hávaði. mbl.is. https://www.mbl.is/frettir/innlent/2020/10/06/thetta_var_svakalegur_havadi/.

Krautblatter, M., Funk, D., Günzel, F.K., 2013. Why permafrost rocks become unstable: a rock–ice-mechanical model in time and space. Earth Surf. Process. Landf. 38, 876–887. https://doi.org/10.1002/esp.3374.

Krüger, J., Kjær, K.H., 2000. De-icing progression of ice-cored moraines in a humid, subpolar climate, kötlujökull, Iceland. The Holocene 10, 737–747. https://doi.org/10.1191/09596830094980.

Laplace, P.S., 1806. Traité de mécanique céleste; supplement au dixième livre, sur l'action capillaire. Supplément au dixième livre du Traité de Mécanique Céleste 4, 1–79.

Mauro, G., 2004. Observations on permafrost ground thermal regimes from Antarctica and the italian alps, and their relevance to global climate change. Glob. Planet. Chang. 40, 159–167. https://doi.org/10.1016/S0921-8181(03)00106-1.

Milana, J.P., 2016. Molards and their relation to landslides involving permafrost failure. Permafr. Periglac. Process. 27, 271–284. https://doi.org/10.1016/j.epsl.2019.03.040.

Morino, C., 2018. The Hidden Hazard of Melting Ground Ice in Northern Iceland. Ph.D. thesis.. The Open University. United Kingdom. https://doi.org/10.21954/ou.ro.0000e1ec.

Morino, C., Conway, S.J., Sæmundsson, Helgason, J.K., Hillier, J., Butcher, F.E., Balme, M.R., Jordan, C., Argles, T., 2019. Molards as an indicator of permafrost degradation and landslide processes. Earth Planet. Sci. Lett. 516, 136–147. https://doi.org/10.1016/j.epsl.2019.03.040.

Morino, C., Conway, S., Philippe, M., Peignaux, C., Svennevig, K., Lucas, A., Noblet, A., Roberti, G., Butcher, F., Collins-May, J., 2023. Permafrost molards as an analogue for ejecta-ice interactions at hale crater, mars. Icarus 391, 115363. https://doi.org/10.1016/j.icarus.2022.115363.

Niu, F., Luo, J., Lin, Z., Fang, J., Liu, M., 2016. Thaw-induced slope failures and stability analyses in permafrost regions of the Qinghai-Tibet plateau, China. Landslides 13, 55–65. https://doi.org/10.1007/s10346-014-0545-2.

Óðinsson, Ó.S., 2020. Enn hætta á skriðum í eyjafirði. RÚV-The Icelandic National Broadcasting Service. URL: https://www.ruv.is/frettir/innlent/2020-10-09-enn-haetta-a-skridum-i-eyjafirdi.

Patton, A.I., Rathburn, S.L., Capps, D.M., 2019. Landslide response to climate change in permafrost regions. Geomorphology 340, 116–128. https://doi.org/10.1016/j.geomorph.2019.04.029.

Philippe, M., Conway, S.J., Font-Ertlen, M., Morino, C., Bourgeois, O., 2021. Link between molards and permafrost degradation: an experimental study. In: EGU General Assembly Conference Abstracts, p. EGU21-8268.

Riseborough, D., Shiklomanov, N., Etzelmüller, B., Gruber, S., Marchenko, S., 2008. Recent advances in permafrost modelling. Permafr. Periglac. Process. 19, 137–156. https://doi.org/10.1002/ppp.615.

Rist, A., Phillips, M., 2005. First results of investigations on hydrothermal processes within the active layer above alpine permafrost in steep terrain. Norsk Geografisk Tidsskrift-Norwegian Journal of Geography 59, 177–183. https://doi.org/10.1080/00291950510020574.

Rivière, A., Jost, A., Gonçalvès, J., Font, M., 2019. Pore water pressure evolution below a freezing front under saturated conditions: Large-scale laboratory experiment and numerical investigation. Cold Reg. Sci. Technol. 158, 76–94. https://doi.org/10.1016/j.coldregions.2018.11.005.

Sæmundsson, Þ., Morino, C., Helgason, J.K., Conway, S.J., Pétursson, H.G., 2018. The triggering factors of the móafellshyrna debris slide in northern Iceland: intense precipitation, earthquake activity and thawing of mountain permafrost. Sci. Total Environ. 621, 1163–1175. https://doi.org/10.1016/j.scitotenv.2017.10.111.

Sæmundsson, Þ., Morino, C., Conway, S.J., 2022. 5.22- mass-movements in cold and polar climates. In: Shroder, J.J.F. (Ed.), Treatise on Geomorphology, Second edition ed. Academic Press, pp. 350–370. https://doi.org/10.1016/B978-0-12-818234-5.00117-6.

Svennevig, K., Hermanns, R.L., Keiding, M., Binder, D., Citterio, M., Dahl-Jensen, T., Mertl, S., Sørensen, E.V., Voss, P.H., 2022. A large frozen debris avalanche entraining warming permafrost ground–the june 2021 assapaat landslide, west greenland. Landslides 19, 2549–2567. https://doi.org/10.1007/s10346-022-01922-7.

Svennevig, K., Keiding, M., Korsgaard, N.J., Lucas, A., Owen, M., Poulsen, M.D., Priebe, J., Sørensen, E.V., Morino, C., 2023. Uncovering a 70-year-old permafrost degradation induced disaster in the arctic, the 1952 niiortuut landslide-tsunami in central West Greenland. Sci. Total Environ. 859, 160110 https://doi.org/10.1016/j.scitotenv.2022.160110.

Tapia Baldis, C., Trombotto Liaudat, D., 2019. Rockslides and rock avalanches in the Central Andes of argentina and their possible association with permafrost degradation. Permafr. Periglac. Process. 30, 330–347. https://doi.org/10.1002/ppp.2024.

Ullman, S., 1979. The interpretation of structure from motion. Proceedings of the Royal Society of London. Series B. Biological Sciences 203, 405–426.

Vedamuthu, M., Singh, S., Robinson, G.W., 1994. Properties of liquid water: origin of the density anomalies. J. Phys. Chem. 98, 2222–2230. https://doi.org/10.1021/j100060a002.

Virtanen, P., Gommers, R., Oliphant, T.E., Haberland, M., Reddy, T., Cournapeau, D., Burovski, E., Peterson, P., Weckesser, W., Bright, J., et al., 2020. Scipy 1.0: fundamental algorithms for scientific computing in python. Nat. Methods 17, 261–272. https://doi.org/10.1038/s41592-019-0686-2.

Wentworth, C.K., 1922. A scale of grade and class terms for clastic sediments. J. Geol. 30, 377–392. URL: https://www.jstor.org/stable/30063207.

Westoby, M.J., Brasington, J., Glasser, N.F., Hambrey, M.J., Reynolds, J.M., 2012. Structure-from-motion'photogrammetry: a low-cost, effective tool for geoscience applications. Geomorphology 179, 300–314. https://doi.org/10.1016/j.geomorph.2012.08.021.

Westoby, M.J., Rounce, D.R., Shaw, T.E., Fyffe, C.L., Moore, P.L., Stewart, R.L., Brock, B.W., 2020. Geomorphological evolution of a debris-covered glacier surface. Earth Surf. Process. Landf. 45, 3431–3448. https://doi.org/10.1002/esp.4973.

Wright, J., Conway, S.J., Morino, C., Rothery, D.A., Balme, M.R., Fassett, C.I., 2020. Modification of caloris ejecta blocks by long-lived mass-wasting: a volatile-driven process? Earth Planet. Sci. Lett. 549, 116519 https://doi.org/10.1016/j.epsl.2020.116519.

Young, T., 1832. An essay on the cohesion of fluids. In: Abstracts of the Papers Printed in the Philosophical Transactions of the Royal Society of London, The Royal Society London, pp. 171–172. https://www.jstor.org/stable/107159.

Zhao, D., Wu, S., 2019. Projected changes in permafrost active layer thickness over the Qinghai-Tibet plateau under climate change. Water Resour. Res. 55, 7860–7875. https://doi.org/10.1029/2019WR024969.